On the effects of leading edge vortex generators on an OA209 airfoil

B. Heine*, K. Mulleners, A. Gardner, H. Mai
Deutsches Zentrum für Luft und Raumfahrt (DLR), Bunsenstraße 10, 37073 Göttingen

Leading edge vortex generators have been found to significantly increase the aerodynamic performance of an airfoil under dynamic stall conditions. However, the principle of operation of these devices is still unclear. Therefore static wind and water tunnel experiments as well as CFD simulations have been conducted on a rotary aircraft wing profile OA209. A POD analysis applied to the vector fields generated by PIV measurements showed that the vortex generators break larger flow structures into small scale formations. They are able to decrease the impact of the dynamic stall vortex and decrease the undesirable aerodynamic fluctuations associated with dynamic stall.

Keywords: Vortex generators, dynamic stall, flow visualization, POD

Nomenclature

α	[°]	Angle of attack
α_0	[°]	Mean angle of attack
$\hat{\alpha}$	[°]	Pitch amplitude
b	[m]	Span
c	[m]	Chord length
c_d	[-]	Drag coefficient
c_l	[-]	Lift coefficient
c_m	[-]	Moment coefficient
f_α	[Hz]	Pitching frequency
ω	$[\frac{1}{s}]$	Angular pitch rate, $2\pi f$
k	[-]	Reduced frequency, $\omega c/2U_\infty$
Ma	[-]	Mach number
Re	[-]	Reynolds number
U_∞	$[\frac{\mathrm{m}}{s}]$	Free stream velocity

I. Introduction

The high speed characteristics of rotary wing aircraft is limited by two factors: transonic flow at the tip of the advancing blade and stall at the retreating blade. While at the advancing blade rotational and forward speeds add up, the retreating blade faces low velocities and even

*Corresponding author: benjamin.heine@dlr.de, Tel.: +49 551 709 2419

reverse flow. To maintain constant lift over the entire rotor disc, high angles of attack are necessary for the retreating blade. The rotor blade therefore has to perform a pitching motion. At a certain forward speed, stall occurs at some part of the retreating blade. Compared to the static stall case, maximum lift and stall angle are delayed due to the dynamic pitching movement of the blade. This phenomenon, referred to as dynamic stall, leads to a series of complicated aerodynamic mechanisms and has been studied by numerous researchers [1–3]. In most cases it induces an abrupt decay and fluctuation of the aerodynamic loads, resulting in high structural loads, drag, noise and control forces. Especially the pitching moments can cause fatal aeroelastic flutter with negative damping. Dynamic stall is therefore considered to be a limiting factor for the helicopter's forward flight performance, but also for the aeroelastic stability of e.g. wind turbines. McCroskey [1] and Carr *et al.* [2] performed comprehensive studies on the phenomenon of dynamic stall and found a concentrated spanwise vortex as the dominant flow structure. For airfoils where leading edge stall occurs, a strong vortex is formed close to the leading edge of the airfoil and travels downstream over the airfoil when the dynamic stall angle is reached. During its convective downstream motion, the vortex temporarily induces high lift and often strong negative pitching moments. Since a large amount of kinetic energy is bound in this large vortex, drag is also significantly increased. Counter-rotating vortices from the trailing edge cause the dynamic stall vortex to depart from the airfoil's surface and the flow on the suction side is completely separated. The following downstroke movement hinders the reattachment of the flow, leading to a large hysteresis. Finally, the boundary layer attaches from front to rear and the aerodynamic coefficients return to unstalled values.

Numerous passive and active dynamic stall control devices have been developed and investigated thoughout the last decades. The aim of such control devices is i) to maintain or increase lift, ii) to maintain or reduce drag and iii) to reduce the negative pitch moment peak during one oscillation. Geißler *et al.* [4] investigated an airfoil that could be deformed during one oscillation by moving the leading edge ("droop nose"). A significant reduction of drag and negative pitching moment peaks at constant maximum lift could be reached. Chandrasekhara *et al.* [5] successfully demonstrated the complete elimination of the dynamic stall vortex by dynamically changing the leading edge geometry. However, the deformation of the leading edge geometry can only be achieved by complex mechanisms, strong actuators and a precise control unit which are difficult to implement into a rotor blade that is exposed to high aerodynamic loads and centrifugal forces. Carr *et al.* [6, 7] investigated slotted airfoils and leading edge slat configurations. Although the leading edge slat could successfully avoid the dynamic stall vortex, the aerodynamic performance of the advancing blade is unacceptable. Slotted airfoils were found to increase maximum lift, but at lower angles of attack drag rises clearly. Greenblatt *et al.* [8] applied periodic excitation on a NACA 0015 airfoil under a wide range of excitation frequencies at dynamic stall conditions. While the moment excursions remain, a significant increase in maximum lift and reductions in drag could be obtained. Post *et al.* [9] investigated active flow control on a pitching airfoil with open- and closed-loop controlled plasma actuators. All configurations exhibited an increase in cycle-integrated lift and depending on the control mode, favorable improvement of the pitching moments. Dynamic excitation and plasma actuators are difficult to implement into a rotor blade and susceptible to failure. In case of the plasma actuators the high electromagnetic radiation due to the necessary high voltages might interfere with other systems. In general, applying additional devices onto or into a rotor blade usually increases the structural weight, construction and maintenance costs. It therefore has to be considered whether there is a net advantage at all.

Mai *et al.* [10] developed a very simple, retro-fit capable passive device that improves the aerodynamic performance of a wing under dynamic stall conditions significantly, and only has minor drawbacks for the rest of the envelope. Since the dynamic stall vortex develops close to the airfoil's leading edge, a dynamic stall control device would be most efficient if located close to the vortex's generation. The final dimension of the cylindrical *LEVoGs* (**L**eading **E**dge

Vortex **G**enerators) was found after a parameter study where spacing, height and diameter were optimized [10]. The best results were achieved using LEVoGs with a height of 0.54 mm and a diameter of 6 mm. In spanwise direction they were spaced equidistantly at 20mm slightly below the leading edge of the airfoil. The LEVoGs were made from self-adhesive rubber and were simply glued onto an existing wing or blade.

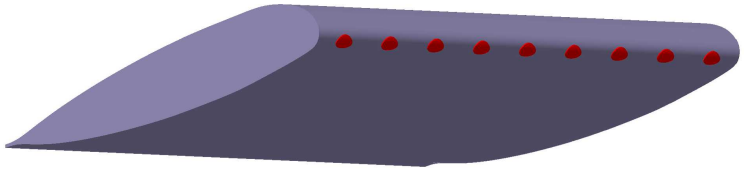

Figure 1. Drawing of the airfoil with LEVoGs.

In figure 1 a drawing of the OA209 airfoil with LEVoGs is depicted. Positioned in the stagnation point of moderate angles of attack, the LEVoGs do not impact the flow field. However, as the angle of attack increases, the stagnation point moves in direction of the trailing edge on the lower side. As a consequence, the LEVoGs are exposed to the flow and become active. Mai *et al.* assumed that the LEVoGs induce streamwise vortices at high angles of attack that entrain high momentum free stream fluid towards the airfoil's surface such that the large scale dynamic stall vortex is split into smaller structures. The less pronounced dynamic stall vortex causes a reduction of the separated flow region and leads to a smaller drag rise and avoids strong negative pitching moments. However, this has not been verified experimentally and is an important task in order to further optimize such vortex generators. In order to understand the aerodynamic mechanisms of such vortex generators, different approaches were chosen:

- PIV[1] measurements in a wind tunnel with an open test section.
- Static PIV measurements and dye flow visualizations in a closed water tunnel.
- Static RANS[2] calculations.

II. Wind tunnel experiments

Wind tunnel experiments to visualize the principle of operation of the LEVoGs were conducted at the 1m wind tunnel (1MG) at the DLR in Göttingen. It has an open test section with dimensions 1.0 m x 0.7 m x 1.4 m (W x H x L). The tunnel has a contraction ratio of 4.8 and allows for a range of subsonic velocities from U_∞=0 - 55 m/s at a turbulence level of 0.15 %. The Mach numbers of Mai's experiments could not be reached in this facility. The open test section is advantageous because of the good optical access. The airfoil was mounted onto the same pitching test bench as used by Mai *et al.* and Mulleners *et al.* [11]. Two hydraulically driven exciters operate in phase, allowing pitch angles up to $\alpha = \alpha_0 \pm 20° \sin \omega t$ at a wide range of oscillating frequencies.

A. Wind tunnel model

The same model of the OA209 airfoil, previously used by Mai *et al.* and Mulleners *et al.*, was subject to the present wind tunnel studies. The wing model has a span b of 1m and a chord length c of 0.3 m, leading to an aspect ratio Λ of 3.33. The airfoil has a relative thickness of 9 % and a relative nose radius of $r_{LE} = 0.01185$ %, or 3.6 mm with regard to the present case. It is equipped with 45 Kulite XCO-093 differential dynamic pressure transducers that were placed

[1] **P**article **I**mage **V**elocimetry
[2] **R**eynolds **A**veraged **N**avier-**S**tokes equations

at mid-chord on the pressure and suction side. The spacing of the pressure transducers was reduced in the leading edge region where high pressure gradients are expected. An integration of the pressure data allowed the determination of lift and pitching moments. The accuracy of the pressure measurements was estimated to be $\pm 0.5\,\%$. Since the chord-based Reynolds number of the wind tunnel experiment is of the same order of magnitude as the full scale case, no trip strip was applied for transition. The axis of rotation of the airfoil was at $x = \frac{c}{4}$ and $z = 0$.

B. Particle Image Velocimetry

To study the impact of the LEVoGs on the flow, PIV measurements were conducted. A frequency doubled Nd:YAG laser ($\lambda = 532\,\mathrm{nm}$) and a plano convex cylindrical lens provided a light sheet that was positioned parallel to the pitch axis by mirrors. DEHS[4] aerosol particles were generated by a Laskin nozzle particle generator with a mean diameter of about $1\,\mu\mathrm{m}$. The particles were recorded by a PCO4000 camera with a resolution of 4008 x 2672 pixels and various focal length lens (85 mm, 170 mm, 340 mm). Figure 2 shows a sketch of the PIV setup. During the experiments numerous light sheet angles (with respect to the pitch axis) at various x-positions were investigated. Besides static measurements, phase locked dynamic measurements with reduced pitching frequencies of $k = 0.05$ and $k = 0.1$ at $\alpha = 18° \pm 8° \sin \omega t$ were also performed. During every fifth period, one PIV double image was recorded. All experiments

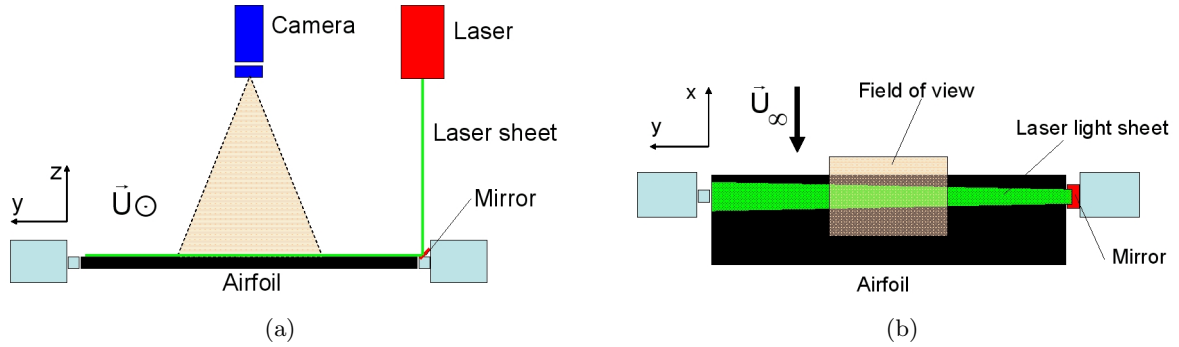

Figure 2. PIV setup in the wind tunnel: a) View from the front, b) view from above.

were conducted at a free stream velocity of U_∞=50 m/s, corresponding to a Reynolds number of Re=930,000 and a Mach number of Ma=0.15. Dynamic experiments were conducted at deep stall conditions ($\alpha = 18° \pm 8° \sin \omega t$) with pitching frequencies of $f_\alpha = 2.65\,\mathrm{Hz}$ and $f_\alpha = 5.3\,\mathrm{Hz}$. For statistic purposes 200 pictures were recorded for every measurement point.

III. Water tunnel experiments

In order to investigate the effects of the LEVoGs in detail, static water tunnel dye visualization experiments and stereoscopic PIV measurements were conducted at the University of Arizona. The closed circuit water tunnel provides a test section length of 4.5 m, a height of 0.8 m, a width of 0.7 m and a maximum tunnel speed of 1.22 m/s. Figure 3 shows a side view of the water tunnel. A honeycomb structure and several screens are positioned upstream of the test section in the settling chamber to straighten and smooth the flow, allowing a turbulence level of below 1 % with a model installed in the test section. A water reservoir located above the test section ensures a constant static pressure. Due to the limited optical access in the test section, measurements and visualizations could only be conducted in the y-plane (perpendicular to the pitch axis).

[4] **D**i-**E**thyl-**H**exyl-**S**ebacate

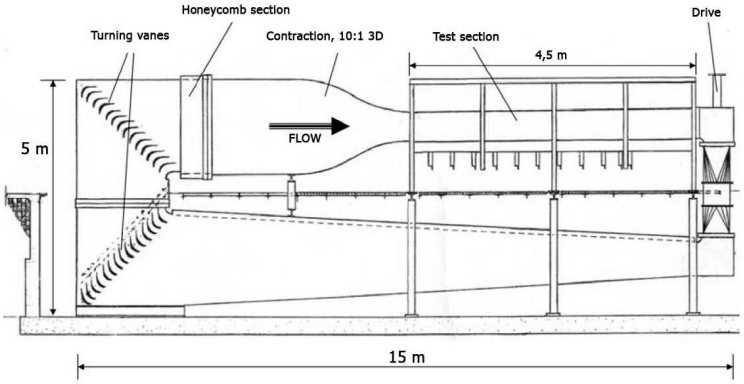

Figure 3. Sketch of the water tunnel at the Hydrodynamics Lab of the University of Arizona.

A. Water tunnel model

A fiberglass model of the OA209 airfoil with a span b of 0.7 m and a chord length c of 0.3 m was built. The model was mounted horizontally onto sealed, turnable discs in the water tunnel windows, which allowed simple variation of the angle of incidence. The wing was mounted flush with the water tunnel walls. The rather large chord length was selected to reach Reynolds numbers in the order of magnitude of the wind tunnel experiments. However, the maximum Reynolds number was still a factor of 2.27 lower than in the wind tunnel experiments. Because of the lower Reynolds number, the height of the LEVoGs was scaled with the boundary layer thickness (flat plate assumption):

$$\frac{\delta_2}{\delta_1} = \frac{h_2}{h_1} = \frac{Re_1}{Re_2} = 2.27 \tag{1}$$

B. Dye Flow Visualization

During the manufacturing process of the OA209 airfoil model, a plastic tube (10 mm diameter) was integrated into the leading edge of the airfoil, extending over the entire span of the wing. For dye flow visualizations, holes of diameter 0.9 mm were drilled perpendicular to the surface and the plastic tube was fed with dye. The dye could be inserted into the flow at different spanwise positions ($y = 0$, $y = c/4$) and different positions relative to the LEVoGs. Two different Reynolds numbers were investigated, the maximum Reynolds number of 410,000, corresponding to the maximum tunnel velocity and a low Reynolds number case (Re=97,000) for better optical acquisition.

C. Stereoscopic Particle Image Velocimetry

Additionally, stereoscopic PIV measurements were performed (Fig. 4), using two PCO cameras with a resolution of 1600 x 1200 pixels placed upstream of the model. The maximum spatial resolution was 7 pixels per millimeter and the size of one interrogation window was 32 x 32 pixels. The cameras, equipped with Scheimpflug adapters, were placed symmetrically with respect to the xz-plane of the model, each looking under an angle of 25° towards the center of the wing. A double pulsed Nd:YAG laser was used to illuminate the tracer particles (hollow glass spheres). Since there was no optical access through the top of the water tunnel, the laser light was directed from the side onto a 45° inclined mirror that is implemented in the water tunnel downstream of the test section. The resulting laser sheet had a thickness of approximately 2mm and was placed perpendicular to the pitch axis.

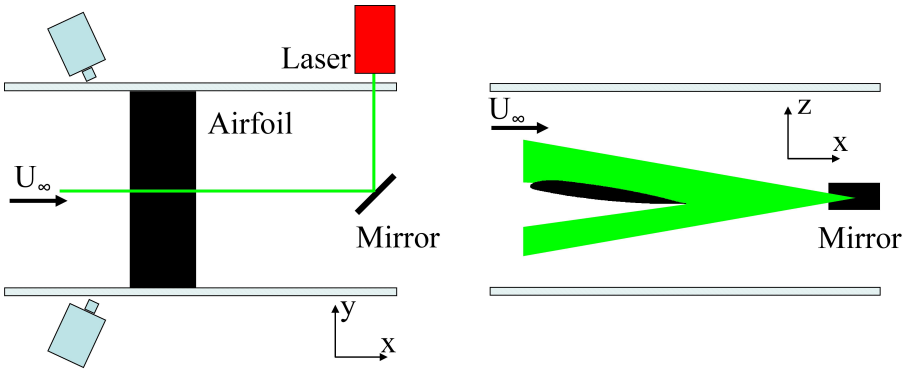

Figure 4. Sketch of the stereoscopic PIV setup in the water tunnel.

IV. Results

A. Dye flow visualization

To get an impression of the difference between the flow around the clean airfoil and the one with LEVoGs, dye flow visualization was performed. Figure 5 shows both configurations of the OA209 airfoil in the water tunnel at different angles of attack. The dye is injected between two LEVoGs at the model mid-span. At low angles of attack, no influence of the LEVoGs on transition and separation could be found, the flow is attached and essentially identical for both cases. Whereas at the clean wing leading edge stall occurs in an abrupt manner at $\alpha \approx 16°$, the flow stays attached in the leading edge region longer if LEVoGs are applied. Separation then moves gradually towards the leading edge, resulting in leading edge stall at about $\alpha = 26°$. Note that for the configuration with LEVoGs, maximum lift is already reached far before leading edge stall occurs. In an attempt to visualize potentially present chordwise vortices, the position of the dye ports (below, above, beside and between two LEVoGs), the angle of attack and the Reynolds number were varied. Especially for the case where 2 dye ports were placed on both sides of a LEVoG at the mid-span position at high angles of attack and low Reynolds number, vortices could be visualized. However, due to the difficult optical access in the water tunnel, it remains unclear whether or not these vortices were spanwise oriented and induced by the LEVoGs.

B. Pressure measurements

Data from the results of the pressure measurements clearly show the effects of the LEVoGs on the airfoil performance under dynamic stall conditions. Figure 6 depicts the lift and moment curves as a function of angle of attack. During the measurements, up to 1000 samples per angle of attack and pressure port were taken. At a pitching frequency of $f_\alpha = 2.65\,\mathrm{Hz}$ and for $\alpha = 18° \pm 8 \sin \omega t$ the positive influence of the LEVoGs is significant. Lift during the downstroke is 43 % higher than for the clean case and the negative pitch moment peak could be reduced by 41 %. Also for the static measurements the influence of the LEVoGs is noticeable (Fig 7). The vortex generators allow the flow to stay attached longer and as a consequence reach a higher maximum lift. In addition, the stall behavior is rather smooth and lift values in the post stall regime are higher than for the clean configuration. The rms value error bars in this region indicate strong pressure fluctuations which represent the highly unsteady characteristics of the flow that is most likely responsible for the better post-stall performance. An analysis of the unsteady pressure measurements on different pressure ports reveal the origin of these strong fluctuations. The separation point shows a strong movement with respect to time, resulting in large differences in lift. The pressure distribution also shows some attached flow in the leading edge region that is lost if the angle of attack is increased further and the lift value of the clean airfoil is reached. Although the observations made in the wind- and water tunnel

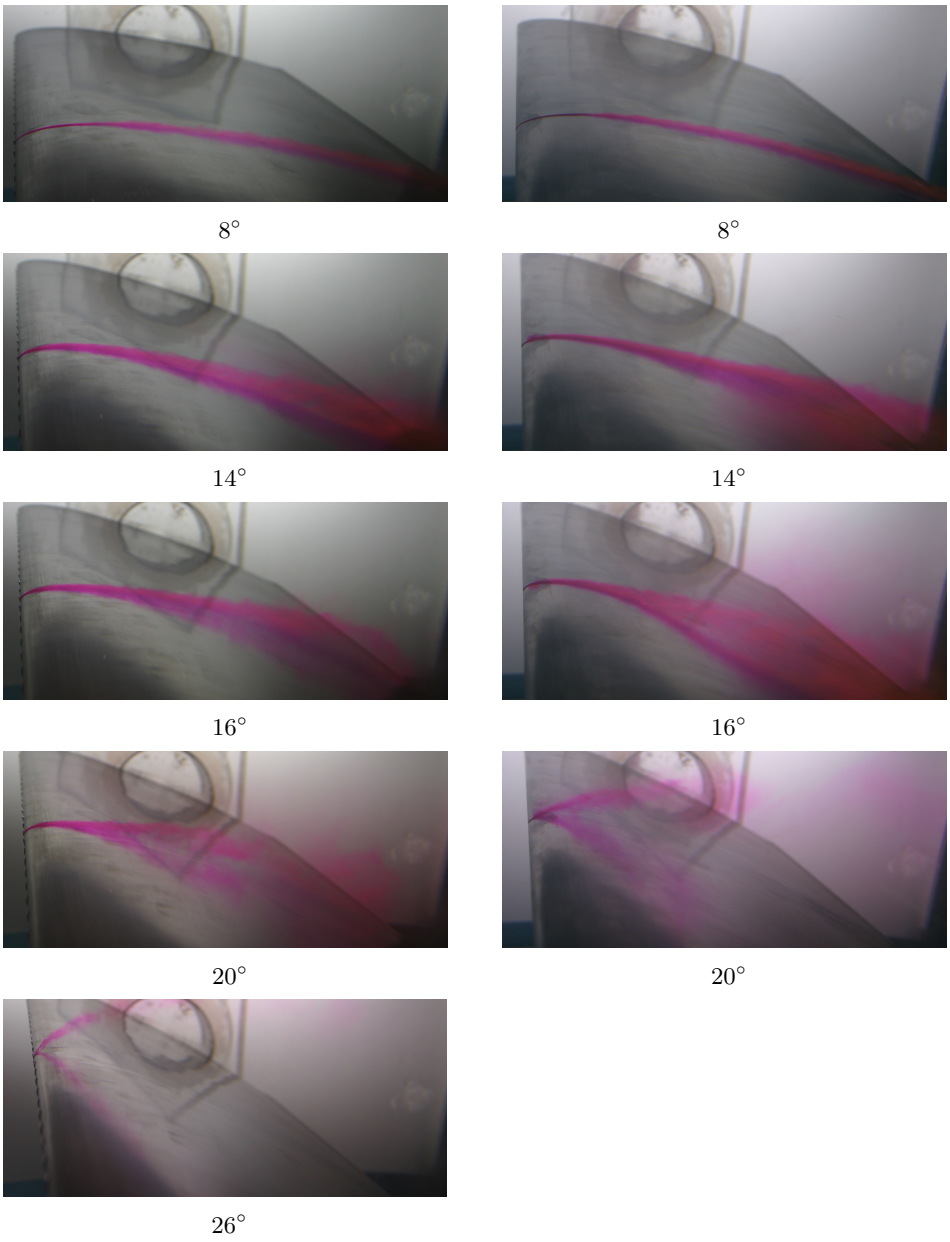

Figure 5. Dye flow visualization of the OA209 airfoil in the water tunnel. The left column represents the cases with LEVoGs, the right column the clean cases.

can not be compared quantitatively since no corrections have been applied, the results are in good agreement (Fig 8). Even beyond the static stall angle the LEVoGs cause the flow to stay attached in the leading edge region, generating a noticeable amount of lift. This lift disappears once leading edge stall is reached. Positive influences on lift could be achieved with the LEVoGs, whereas the moment curve depicts a higher negative pitching moment after stall.

C. PIV measurements

Detecting the structures generated by the LEVoGs with PIV was more challenging than originally assumed. The expected vortical structures have not been found to be stable and well pronounced, but rather to be diffuse and at varying smaller scales. Additionally, due to the limited resolution obtained during the test, quite some effort was required in order to detect the effects of the LEVoGs with PIV in the wind tunnel, and several different setups were tested. In none of the experiments could actual vortices be detected, however the impact of the LEVoGs on the flow could be visualized for static and dynamic measurements. Figure 8 shows a compar-

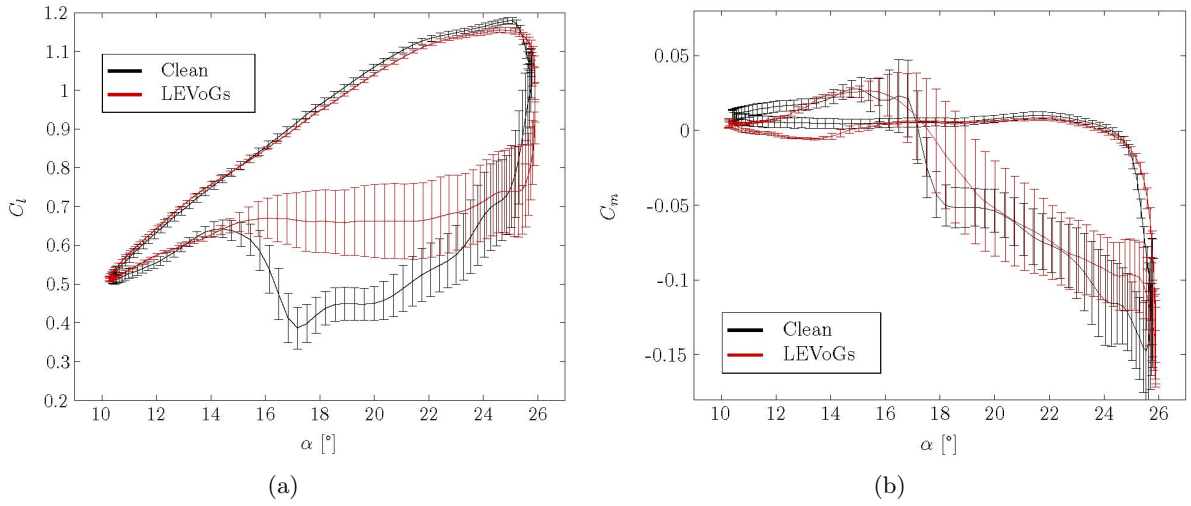

Figure 6. Dynamic lift and moment curves plotted over angle of attack for clean and LEVoG configuration at $f_\alpha = 2.65$ Hz. Errorbars are RMS values.

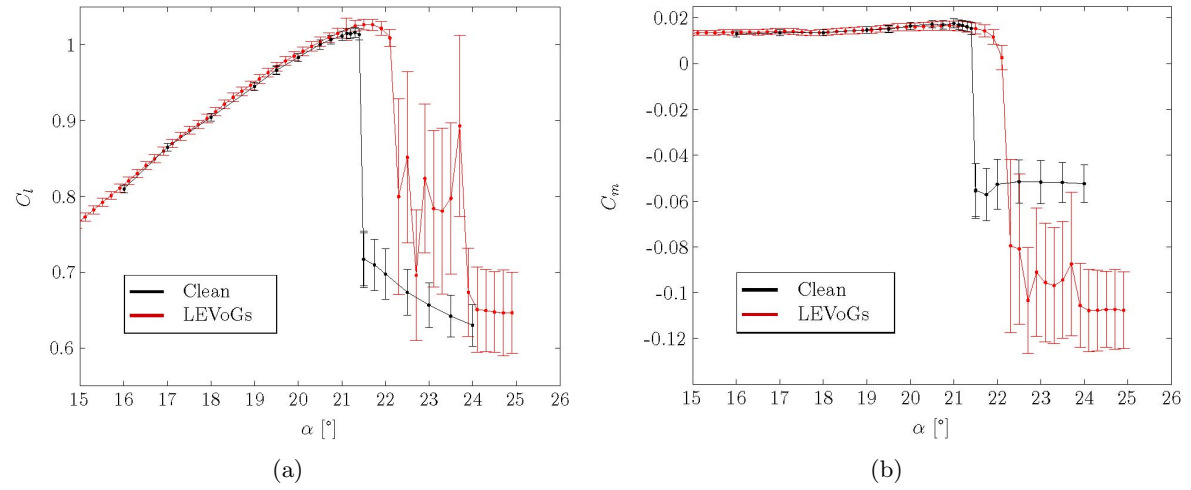

Figure 7. Static lift and moment curves plotted over angle of attack for clean and LEVoG configuration. Errorbars are RMS values.

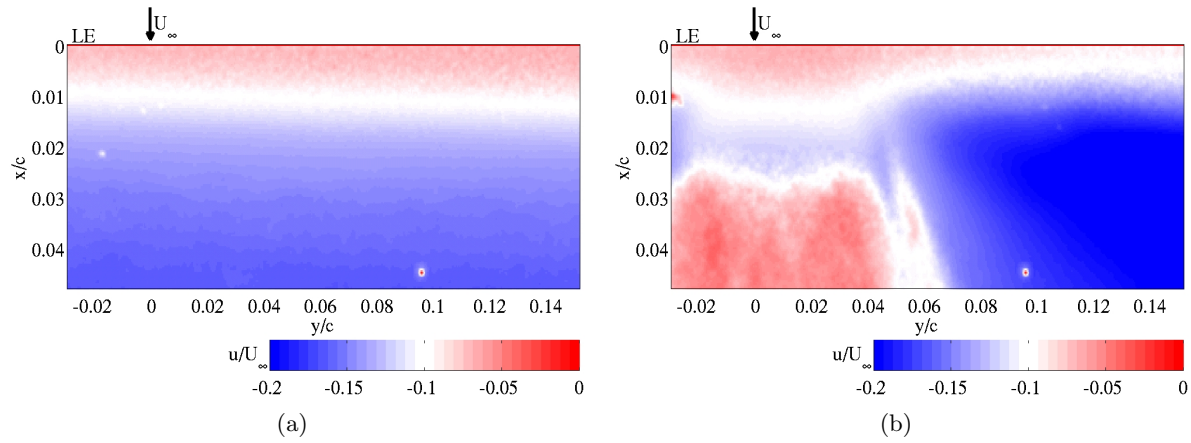

Figure 8. Comparison of the leading edge region at $\alpha = 28°$ (static): a) with LEVoGs, b) Clean wing configuration.

ison between a ensemble correlated velocity field of respectively the clean wing and the LEVoGs configuration at the nose of the OA209 airfoil (static measurement). The spatial resolution of the recorded image is 60 pixels per millimeter, whereas the grid spacing was 0.2 millimeter. The field of view is parallel to the pitch axis and rotated 70° with respect to the horizontal. The light sheet is very close to the surface, but it is not touching the wing. In figure 8(b) the onset of stall is clearly visible by the decreased local velocity, whereas in figure 8(a) the velocity distribution is still homogenous.

In another experiment the light sheet was positioned closer to the surface, such that the tips of the LEVoGs were illuminated. This, in combination with a decreased angle of the flight sheet, allowed the visualization of the wake or "footprints" of the LEVoGs in the ensemble correlated measurements. The spatial resolution was 15 pixels per millimeter. Figure 9 depicts the spanwise velocity component v of the flow around the pitching airfoil at $f_\alpha = 2.65$Hz and $\alpha \approx 20°$. The difficulties in capturing the vortices generated by the LEVoGs with PIV are

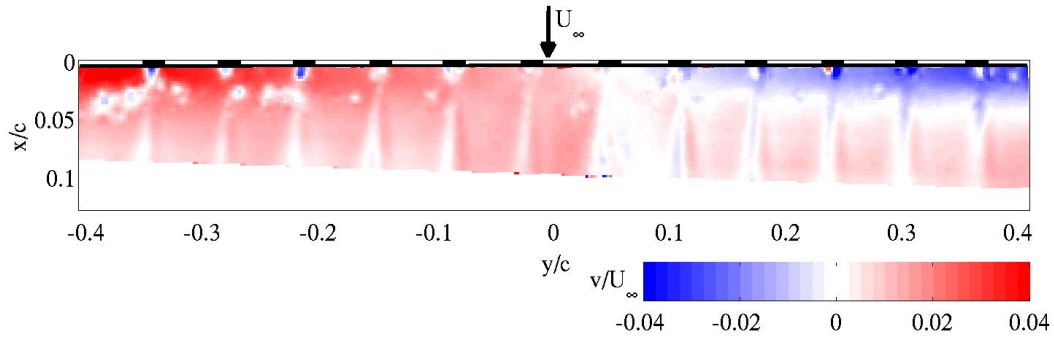

Figure 9. Spanwise velocity component of the ensemble correlated dynamic measurement at $f_\alpha = 2.65$Hz and $\alpha \approx 20°$.

apparently caused by the small scale of the structures, the intricate optical access for the laser sheet (small leading edge radius), surface reflections and difficulties seeding the boundary layer with particles. In summary it can be stated, that the wake of the device in the boundary layer is more turbulent and randomly varying than a steady vortical structure.

The results of the stereoscopic PIV measurements in the water tunnel confirm the previously discussed observations made with the dye visualization, and wind tunnel experiments. Unfortunately, liquid prisms to reduce the distortion effects created by the pass through air, thick plexi-glass and water were not available. These distortion effects and the low spatial resolution did not allow the capture of the small structures created by the LEVoGs.

D. Proper Orthogonal Decomposition

To analyze on how the energy is distributed in the flow field, the *Proper Orthogonal Decomposition* (POD) method was used for postprocessing and applied to $n_{snap} = 300$ vorticity fields per angle of attack. Since the LEVoGs become active only at higher angles of attack, three cases from moderate trailing edge separation to the onset of stall were chosen for the POD analysis. Figure 10 depicts the energy spectra at angles of incidence of 14°, 15° and 16°. It is obvious that for all cases the lower eigenmodes of the clean configuration contain more energy than those of the LEVoG configuration. As assumed by Mai *et al.*, the vortex generators apparently break the larger flow structures into smaller ones. Figure 11 confirms this observation, it shows the energy distribution of two modes at $\alpha = 15°$. Whereas in the clean cases large structures prevail in the dominant modes, only small structures can be seen in the dominant modes corresponding to the configuration with LEVoGs. The smaller structures help the flow to overcome stronger adverse pressure gradients and stay attached longer (compare Fig. 5). For the dynamic case, this effect is expected to reduce the influence of the dynamic stall vortex.

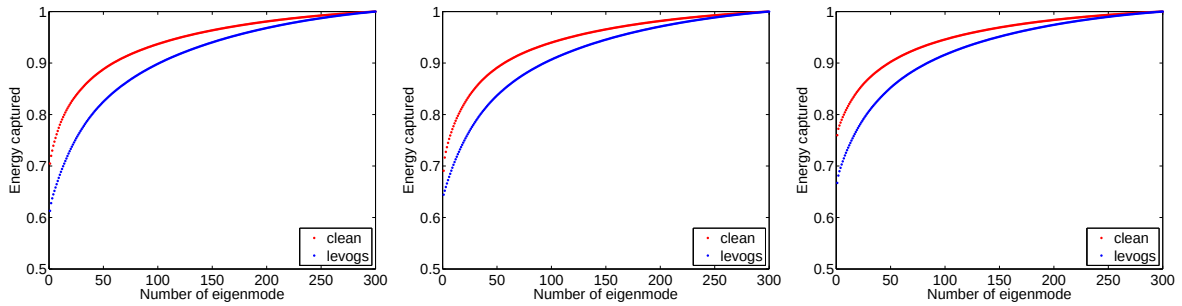

(a) (b) (c)

Figure 10. Normalized energy spectrum (cumulative sum) generated with POD at 3 different angles of attack a) $\alpha = 14°$**, b)** $\alpha = 15°$**, c)** $\alpha = 16°$**.**

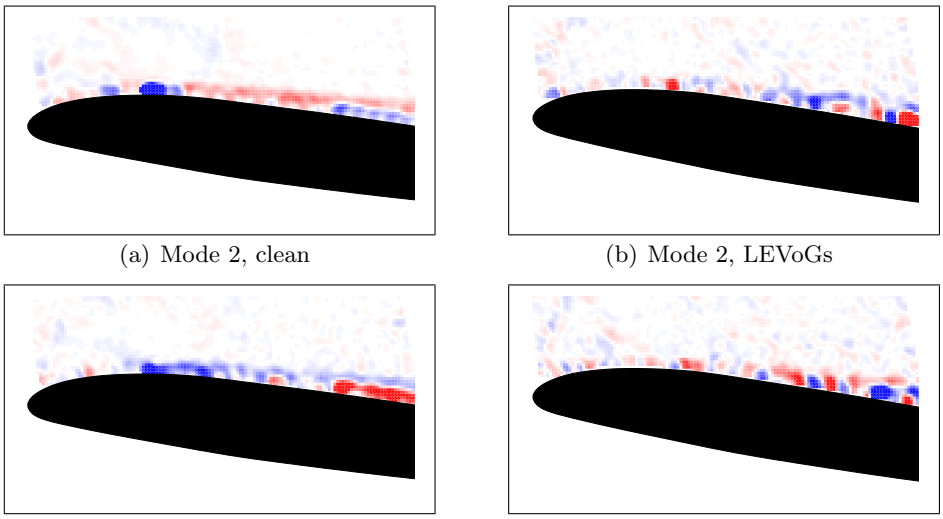

(a) Mode 2, clean (b) Mode 2, LEVoGs

(c) Mode 3, clean (d) Mode 3, LEVoGs

Figure 11. Dominant modes of the decomposition at $\alpha = 15°$**.**

V. CFD Calculations

A computational fluid dynamics study with a RANS code was also performed for static angles of attack. The DLR TAU flow solver [12] and the grid generation software Centaur^{TM}was used to predict the aerodynamic characteristics of the two configurations. In the finite volume solver the one-equation Spalart Allmaras (SAO) turbulence model was used. The airfoil was modeled with an aspect ratio Λ of 1 with symmetric wall boundaries. The circular farfield has a radius of 500 chord lengths and the computational domain has a total number of 1.3-million grid points. Seven angles of attack between $\alpha = 5°$ and $\alpha = 17°$ were calculated for each configuration. For all cases the free stream Mach number Ma was 0.31 at a Reynolds number Re of 1,150,000, representing realistic values. The position of the laminar-turbulent transition was fixed according to the predictions of the simple panel method code XFoil [13]. Streamtraces in the simulated flow field of the simulation shed some light on the principle of operation of the vortex generators. Figure 12a) shows the wing at $\alpha = 17°$ with the surface pressure distribution and streamtraces. The streamtrace ribbons passing the LEVoGs get twisted in chordwise direction, indicating chordwise vortices. Figure 12b) shows a close-up of the leading edge with a cutting plane normal to the airfoils's surface just above the LEVoGs. In the normal cutting plane the helicity distribution is plotted, where red color indicates clockwise rotation and blue indicates counter-clockwise rotation. For every LEVoG, a pair of such weak rotating structures can be found. However, the effects are no proof of longitudinal vortices and they dissipate quickly. This can be attributed to a rather coarse mesh in the wake of the LEVoGs.

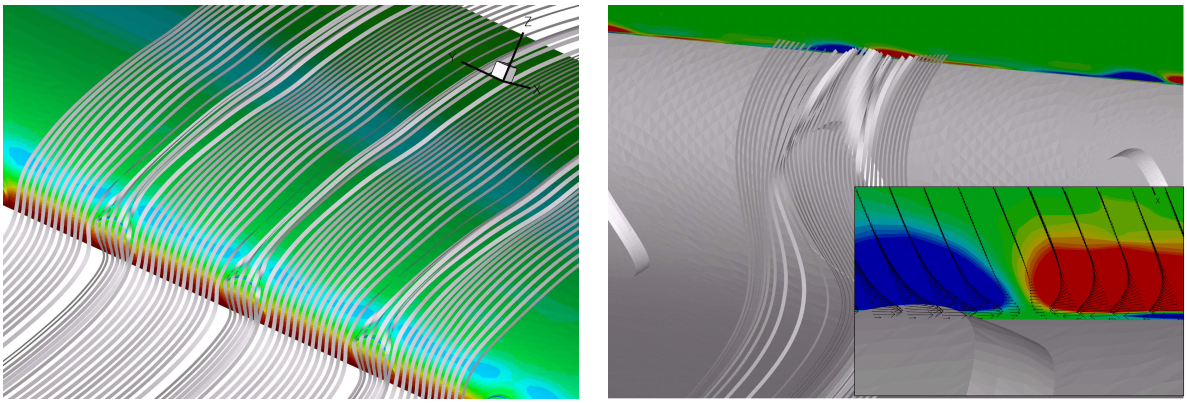

(a) (b)

Figure 12. Streamtraces of the flow around LEVoGs at $\alpha = 17°$. a) Leading edge region with surface pressure distribution, b) Helicity in normal plane downstream of the LEVoGs.

In order to get a better resolution of these effects a different grid and possibly time resolved simulations are necessary. At $\alpha = 17°$ the angle of attack is past stall, but as observed in the previous experiments, the flow doesn't separate right from the leading edge. After stall, the flow around the LEVoG configuration does not drift as far away from the airfoil's surface as in the clean case. It is also remarkable that in the simulation the leading edge separation bubble only disappears when leading edge stall is reached. Figure 13 shows λ_2 iso-surfaces for both configurations at $\alpha = 17.5°$. The vortical "footprint" of the LEVoGs can be clearly observed with this vortex criterion. The iso surfaces show λ_2-bubbles at high angles of attack that indicate the presence of strong, local, vortical structures.

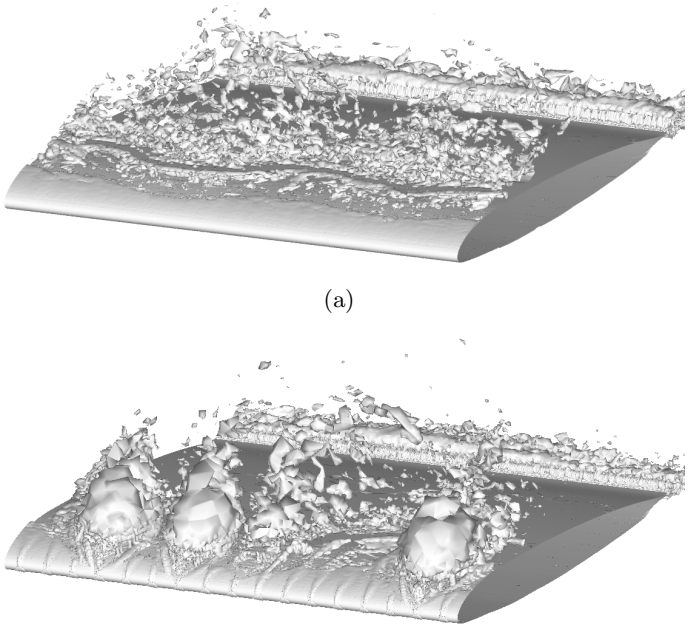

(a)

(b)

Figure 13. λ_2 vortex definition for a) clean and b) LEVoG case at $\alpha = 17.5°$.

VI. Conclusion & Outlook

The principle of operation of leading edge vortex generators on an OA209 airfoil has been investigated, employing wind- and water tunnel experiments as well as CFD simulations. Mai *et al.* assumed that these LEVoGs create chord wise vortices that diminish the influence of the dynamic stall vortex. Unsteady pressure measurements in the wind tunnel showed a significant improvement of the airfoil's performance under dynamic stall conditions if the LEVoGs are applied, however it was not possible to visualize the spanwise vortices with PIV measurements techniques and dye flow visualizations. Further analysis of the PIV measurements were performed with the POD snapshot method. These investigations revealed that the vortex generators break larger flow structures into smaller formations, allowing the flow to overcome higher adverse pressure gradients and potentially reduce the influence of the dynamic stall vortex. The CFD simulations performed showed chordwise vortical structures and the formation of locally confined stall "bubbles" between the LEVoGs at very high angles of attack. In order to gain better insight into the small flow structures behind the LEVoGs, fundamental experiments on a simple circular cylinder are planned. In addition, 3D unsteady RANS simulations for static angles of attack will be calculated with the DLR TAU code. Only when the flow phenomena are fully understood, can the shape, position and size of such vortex generators be properly optimized.

Acknowledgements

This work was supported and funded by the common DLR and ONERA rotorcraft research programme SIMCOS (Advanced Simulation and Control of Dynamic Stall). The authors would like to thank Prof. Dr. Fasel (The University of Arizona) and Prof. Dr. Raffel (DLR Göttingen) for the excellent cooperation and support.

References

[1] McCroskey, W., "The Phenomenon of Dynamic Stall," *NASA TM-81264*, 1981.

[2] Carr, L., "Analysis of the Development of Dynamic Stall Based on Oscillating Airfoil Experiments," *NASA TN-8382*, 1977.

[3] Leishman, J., "Dynamic Stall Experiments on the NACA 23012 Aerofoil," *Experiments in Fluids*, Vol. 9, No. 1, 1990, pp. 49–58.

[4] Geißler, W. and M., R., "Dynamic Stall Control by Airfoil Deformation," *19. European Rotorcraft Forum*, Vol. 1, 1993.

[5] Chandrasekhara, M., Wilder, M., and Carr, L., "Unsteady Stall Control Using Dynamically Deforming Airfoils," *AIAA Journal*, Vol. 36, No. 10, 1998, pp. 1792–1800.

[6] Carr, L., Chandrashekara, M., Wilder, M., and Noonan, K., "The Effect of Compressibility on Suppression of Dynamic Stall Using a Slotted Airfoil," *AIAA Paper 1998-332*, 1998.

[7] Carr, L. and McAlister, K., "The Effect of a Leading-Edge Slat on the Dynamic Stall of an Oscillating Airfoil," *AIAA Paper 1983-2533*, 1983.

[8] Greenblatt, D. and Wygnanski, I., "Dynamic Stall Control by Periodic Excitation, Part1: NACA 0015 Parametric Studies," *Journal of Aircraft*, Vol. 38, No. 3, 2001, pp. 430–438.

[9] Post, M. and Corke, T., "Separation Control Using Plsama Actuators: Dynamic Stall Vortex Control on Oscillating Airfoil," *AIAA Journal*, Vol. 44, No. 12, 2004, pp. 3125–3135.

[10] Mai, H., Dietz, G., Geißler, W., Richter, K., Bosbach, J., Richard, H., and de Groot, K., "Dynamic Stall Control by Leading Edge Vortex Generators," *American Helicopter Society*, Vol. 62, 2006.

[11] Mulleners, K., Henning, A., Mai, H., and Raffel, M., "Investigation of the Unsteady Flow Development over a Pitching Airfoil by Means of TR-PIV," *AIAA Paper 2009-3504*, 2009.

[12] Gerhold, T., Friedrich, O., Evans, J., and Galle, M., "Calculation of Complex Three-Dimensional Configurations Employing the DLR-TAU-Code," *AIAA-paper 97-0167*, 1997.

[13] Drela, M. and Giles, M., "Viscous-Inviscid Analysis of Transonic and Low Reynolds Number Airfoils," *AIAA Journal*, Vol. 25, No. 10, 1987.